Neutron detection in mixed short-pulsed fields with intense photon flashes for LINAC-based active interrogation applications

Clément Besnard Vauterin, Benjamin Rapp, Valentin Blideanu

Nuclear Instruments and Methods in Physics Research Section A:
Accelerators, Spectrometers, Detectors and Associated Equipment

Neutron detection in mixed short-pulsed fields with intense photon flashes for LINAC-based active interrogation applications

C. Besnard-Vauterin[1], B. Rapp[1], and V. Blideanu[1]

[1]Université Paris-Saclay, CEA, List, Laboratoire National Henri Becquerel (LNE-LNHB)
F-91129, Palaiseau, France

clement.besnardvauterin@cea.fr, benjamin.rapp@cea.fr, valentin.blideanu@cea.fr

ABSTRACT

High-energy photon interrogation has established itself as a valuable tool for detecting special nuclear materials and characterizing nuclear waste. Previous research predominantly uses around 9-MV linear electron accelerators (LINACs) as photon sources and limited exploration has been conducted on the use of organic scintillators to determine the energy deposited in the detector and to separate photon and neutron radiation, crucial when the photon interrogation is based on the measurement of the neutron emission. The challenge arises from the intense photon flux typically produced by electron accelerators, resulting in issues such as pulse pile-up, detector saturation, and a suboptimal signal-to-background ratio. This study aims to extend the applicability of the conventional Active Photon Interrogation (API) techniques by introducing a novel method enabling the detection, in addition to nuclear materials, of light elements—specifically nitrogen, oxygen, and carbon—known to be present in conventional explosives, narcotics, and chemical weapons. The approach relies on active photon interrogation at high energies above 12 MeV, coupled with photoneutron spectrometry. Using a 22-MV electron LINAC, pulse shape discrimination with an organic liquid scintillator demonstrated promising performance. Our results highlight that the conventional pulse shape discrimination capabilities and rapid time-scale operation of organic scintillators enable the detection of fast neutrons from (γ,Xn) reactions, even in a mixed short-pulsed field of photon and neutron radiation with intense photon flashes. This exploration of the initial experimental aspects of photoneutron detection induced by high-energy photons establishes a foundation for a promising new method for the detection of illicit materials.

KEYWORDS: homeland security, neutron, scintillator, pulse-shape discrimination, LINAC, BC501A

1. INTRODUCTION

The escalating challenges related to international trade growth and the trafficking of illicit materials, including special nuclear materials, conventional explosives, narcotics, and chemical weapons, have heightened the importance of homeland security measures. Non-intrusive on-site inspections are crucial in this context, yet current active interrogation methods face limitations.

Existing techniques fall into two categories based on the probe particles being used. Neutron-induced reactions at the foundation of the active neutron interrogation method are using associated particle techniques (APT) for detecting illicit materials in containers [1, 2]. However, photon spectra measurement in this approach is intricate due to high background levels under typical measurement conditions. Conversely, active photon interrogation (API) currently involves the use of photons around 9 MeV inducing photofission (γ,f) reactions on actinides and so allowing the detection of special nuclear materials (SNM) like uranium and plutonium [3] or the characterization of nuclear waste containers.

Recent advancements allow to extend API capabilities, introducing a novel method for the unprecedented detection of light elements such as nitrogen, oxygen, and carbon in conventional explosives, narcotics, and chemical weapons. This new method employs active photon interrogation at energies exceeding 12 MeV, coupled with photoneutron spectrometry [4, 5]. Unlike traditional neutron interrogation, this technique leverages the penetrating nature of photons, avoiding probe neutron scattering and attenuation related limitations characterizing the APT interrogation methods. For photons below 9 MeV, (γ,f) reactions confirm nuclear material presence through the production of fast neutrons. In contrast, photons with energies exceeding about 12 MeV enable the neutron production for almost all nuclei through photonuclear (γ,Xn) reactions. The reactions at the origin of neutron emission can be further identified by the detailed analysis of the photoneutron energy spectra, namely based on deep learning algorithms [6].

Linear electron accelerators (LINACs) allow the production of Bremsstrahlung photons of high flux, the latter being crucial for the feasibility of the photon interrogation methods. Organic scintillators, with pulse shape discrimination (PSD) capabilities and rapid time-scale operation, proved to be effective in detecting fast neutrons from (γ,f) or (γ,Xn) reactions. Overcoming obstacles however, such as discriminating fast neutrons from interrogating photons and active background signals, as well as detecting a large flux of particles on a short time scale due to the pulsed structure of the electron beam producing the photon source, presently limit the potential of these advancements to enhance the detection capabilities for homeland security applications.

The use of organic scintillators for neutron detection in the context of special nuclear materials has been explored in a limited number of studies related to the interrogation of actinide contents [7-9]. They are predominantly employing linear accelerators with an energy endpoint output around 9 MeV which is sufficient to undergo (γ,f) reactions. While these investigations provided valuable insights, there is still a notable lack in extending such applications to higher photon energies allowing to open (γ,Xn) reaction channels on all elements including the light ones as carbon, nitrogen and oxygen. In this study, we aim to address this gap by exploring for the first time the use of organic scintillators for photoneutron detection using a LINAC with a substantially higher energy output, reaching an energy endpoint maximum of 22 MeV, allowing the emission of photoneutrons from (γ,Xn) reactions. The neutron production from these reactions is significantly lower than from (γ,f) reactions, making the detection of photoneutrons even more challenging when comes to neutron/photon ratio. This endeavor seeks to explore the capability of existing neutron detection methodologies in allowing to broader the applicability of Active Photon Interrogation (API) techniques by including the identification of light elements and so the possibility to detect a large panel of illicit materials for homeland security applications.

2. EXPERIMENTAL SET-UP

2.1. Photon source based on an electron linear accelerator

Our laboratory is equipped with a Varian TrueBeam medical linear electron accelerator, featuring an endpoint energy of 22 MeV. Originally designed for applications in radiotherapy, this accelerator is housed by the DOSEO platform on CEA-Saclay site. The accelerator generates electron pulses with durations ranging from 3 to 4 μs and the pulse frequency is adjustable within the range of a few hertz to 360 Hz. In our experimental setup, the electron beam is directed onto a 1 cm thick natural tungsten target with a width of 10 cm covering the whole electron beam spot at the selected irradiation position, at a distance of 1 meter from the exit point of the accelerator's deviation chamber as illustrated in Figure 1. This allows the most energetic electrons produced by the LINAC to be completely stopped into the target and by doing so, the Bremsstrahlung photons and the subsequent photonuclear reactions leading to the emission of photoneutrons to take place in the same target. The tungsten material has been chosen as photoneutron production target considering its high cross-section for photonuclear (γ,Xn) reactions. This is in line with the main objective of this study, which is to demonstrate the feasibility of neutron detection in the environment specific to high energy pulsed electron accelerators.

Neutron detection in mixed short-pulsed fields with intense photon flashes for LINAC-based active interrogation applications

Modification of the Varian linear electron accelerator for the experiment

Several modifications were needed to make the Varian TrueBeam electron linear accelerator suitable for our experiment, allowing achieving a clean, well-focused, and less intense electron beam tailored to the specificity of the measurements intended. The internal electron-to-photon conversion target for radiotherapy applications was not used. This choice allowed to exclusively work with the electron beam, limiting any photon radiation production inside the accelerator's head that could have led to unwanted photoneutron production. Furthermore, filters used traditionally to scatter the electron beam in the context of radiotherapy treatments have been removed in order to preserve the electron beam focus. Finally, the accelerator's monitoring chamber, which is designed to measure beam position and intensity during standard radiotherapy treatments, has been moved from the beam path in our dedicated setup. This was done to prevent potential damage to the chamber from the focused electron beam, but in exchange it canceled the real-time access to the beam current and intensity data.

Beam intensity optimization to minimize in-detector flash

The electron stripping voltage is a critical parameter that governs the beam intensity. It has been reduced for the purpose of our experiment in order to increase the quality of data acquisition and to preserve the integrity of our experimental setup. Standard value of electron stripping voltage results in an intensity of a few μA (typically 10^{13} electrons/s), which lead to an intense photon radiation signal being registered by the detector as a saturated flash. By lowering this value, we effectively reduced the beam intensity while maintaining the electron energy needed for our experiment. This adjustment allowed a better-controlled and more manageable interaction in the detector. The incidence of disruptive flashes has been significantly reduced, consequently improving the quality of the registered data.

Alternative approach for monitoring the electron beam intensity

Monitoring the beam intensity during irradiation being of a critical importance namely for data normalization, an alternative method has been implemented consequently to the removal of accelerator's monitoring chamber to ensure the accurate measurement of the source term. While lowering the electron stripping voltage successfully curtailed the intensity of the electron beam and reduced flashes in the detector, it added complexity to the direct quantification of the beam intensity since conventional methods originally equipping the accelerator for this purpose (conversion target, monitor chamber) are no longer suitable.

Fig. 1. Picture of the Varian TrueBeam accelerator with the irradiated target.

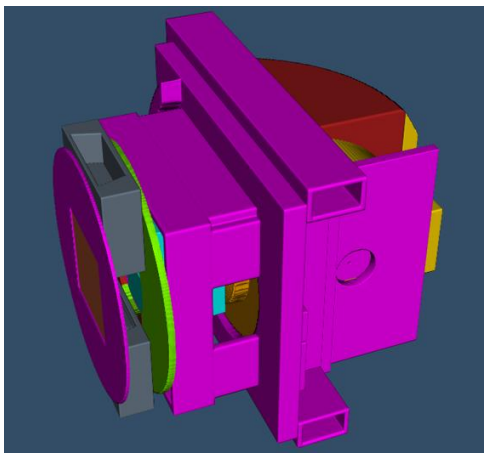

Fig. 2. 3D geometry model of the Varian TrueBeam accelerator for Monte-Carlo simulations with MCNP6.2

To address this challenge, the alternative methodology developed is based on the dose measurements done with previously calibrated GAFchromic EBT-XD films positioned on the electron beam path. This

type of detector is known for its sensitivity to ionizing radiation and usually serve as passive dosimeter namely in radiotherapy applications. A 3 mm thick PMMA plate was placed in front of the GAFchromic film to ensure the electronic equilibrium. The dose deposited in the film by the electron beam has been measured and calculated by Monte-Carlo simulations with MCNP6.2 code accurately reproducing the geometry of the experimental set-up (Figures 1 and 2). It became possible in this way to indirectly determine the electron beam intensity by deducing the source strength in electrons/s to be used for the simulation results presented in Figure 3 in order to reproduce the dose rate values measured by the GAFchromic films (Figure 4). Given the electron pulse duration of 3.5 μs and the frequency used of 120 Hz, the deduced electron beam intensity is of 1.22×10^{10} electrons/s (corresponding to 1.95 nA) which is about 1000 times less than its rated nominal value of the order of several μA. This new method offers a robust and adaptable solution allowing determining the electron beam intensity without relying on the original monitoring systems.

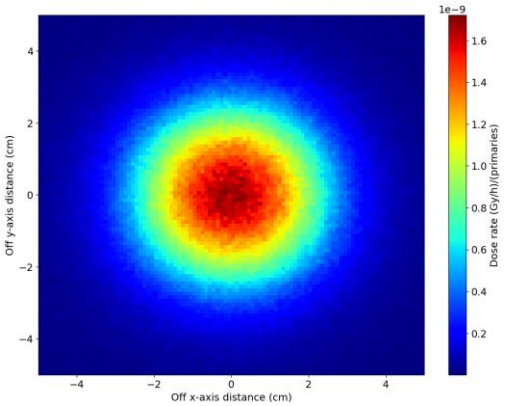

Fig.3 Simulated mesh of the dose rate deposited in the GAFchromic film.

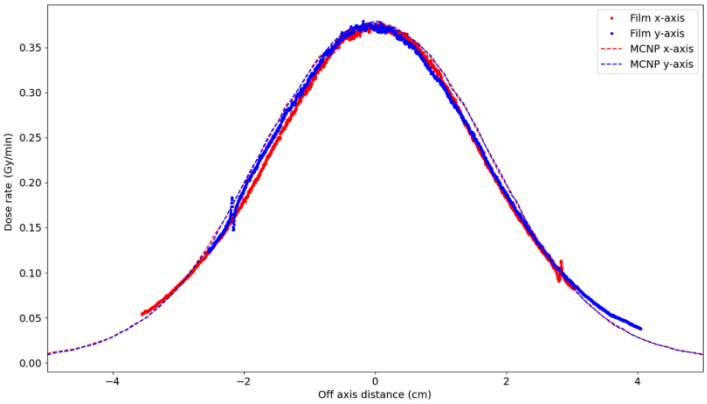

Fig. 4. Measured and simulated dose rate cross-axis profiles in the GAFchromic EBT-XD film.

2.2. Neutron detector set-up and data acquisition

Measurements were done using an organic liquid scintillator BC501A, contained in a cylindrical measurement cell of 5.08 cm of diameter and 5.08 cm of height, composed primarily of Xylene (> 90%) as the solvent and aromatic fluorine (< 10%) as the solute, with a density of 0.874 g/cm^3. BC501A shares similarities with other well-established detectors like NE213 or EJ301, showing good pulse shape discrimination capabilities [10] and so making it suitable for accurate detection of neutrons and photons in mixed n-γ radiation fields. This scintillator allows a fast decay time of 3.2 ns, a valuable characteristic in managing the high particle flux generated during LINAC pulses.

Our detection set-up features a Hamamatsu R329-02 photomultiplier tube (PMT) operated at -1300 V coupled to the scintillator cell, chosen for its fast time response with a 2.6 ns anode pulse rise time. Signal acquisition was facilitated using a CAEN DT5743 digitizer with a 3.2 GHz sampling frequency, an input range of ±1.25 V and a 12-bit resolution. It has been synchronized with an external trigger signal generated by the Varian TrueBeam accelerator and shaped through a LabVIEW counter –timer card. A custom LabVIEW software allows to adjust the length and delay of the output generated signal synchronized with the accelerator one. This synchronized signal serves as an AND gate, applied via the CAEN WaveCatcher software to select detected events occurring within our predefined time frame.

A schematic view of the acquisition chain is depicted in Figure 5. To illustrate the synchronization between the detector's acquisition and LINAC's beam, Figure 6 shows the histogram of timestamps corresponding to events detected throughout the accelerator's pulse. Those events were registered with a WavePro804HD-MS digital oscilloscope with a sampling frequency of 5 GHz. It reveals a noteworthy phenomenon, wherein the pulse exhibits a distinctive wave pattern with an approximate frequency of 2 MHz before attaining stability at the midpoint of the pulse displaying the pulse time structure.

Given the substantial difference in strength between the photon and neutron fields, the detector has been additionally shielded for photons using a front tungsten block of 10 cm of thickness.

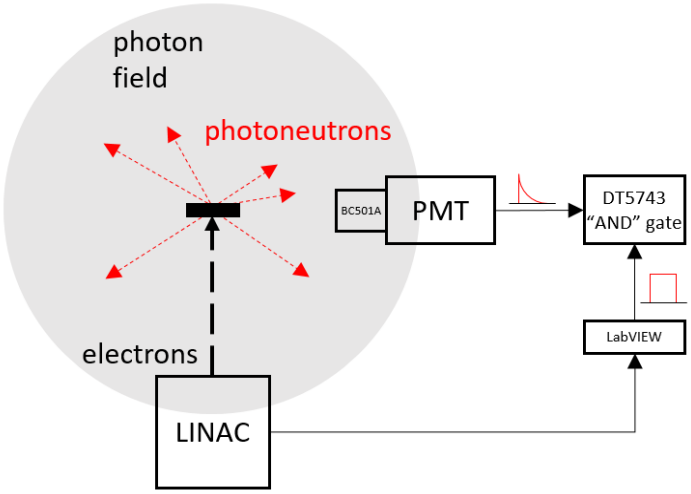

Fig. 5. Schematic of the data acquisition chain.

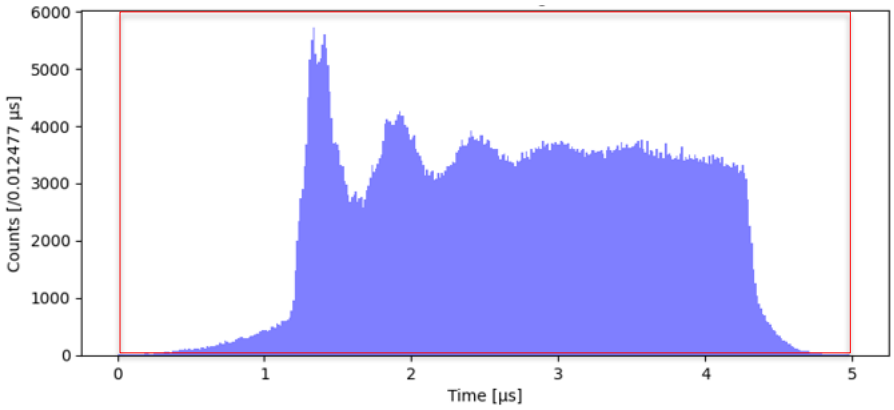

Fig. 6. Histogram of the timestamps of each detected event. The red window represents the synchronisation signal of 5 µs being used.

3. DATA ANALYSIS

3.1. Post-treatment and pile-ups rejection

In neutron-photon discrimination, a robust post-treatment algorithm is crucial for extracting meaningful information from digital pulse shape data, particularly in the dynamic environment of a linear electron accelerator. The challenges include high-speed output pulses, a high frequency of piled-up events and a wide variety of pulse amplitudes due to the wide range of photon energies, which can reach in the case of our experiment a maximum of 22 MeV. Efficient pile-up rejection is essential; therefore, measurements performed in this work with the LINAC required a sophisticated algorithm to address this issue.

Handling high-speed output pulses with a rise time of 10 ns or less can lead to distorted waveforms due to resonance in the photomultiplier electrode structure and to the reactance of the signal output system, including the voltage-divider circuit, as outlined in the Hamamatsu handbook on photomultiplier tubes [12]. To mitigate this distortion, damping resistors, denoted as R27 and R26 each having a value of 100 Ω, are strategically inserted into the last, and if necessary, the next-to-last dynode in the E5859 taper bleeder circuit

of the Hamamatsu R329-02 photomultiplier tube (Figure 7).

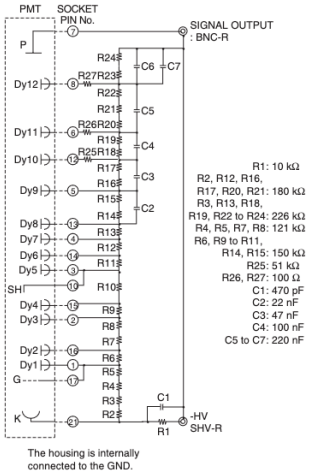

Fig. 7. E5859 Taper bleeder circuit (For R329/R331-05/R6091 PMTs) Schematic taken from [11].

Despite these special precautions however, signals generated by high-energy photons resulting in high amplitudes during our experiments may exhibit some distortion as illustrated in Figure 8. This increases the difficulty for algorithms designed to reject piled-up events while accurately distinguishing single events of distorted high-energy photons.

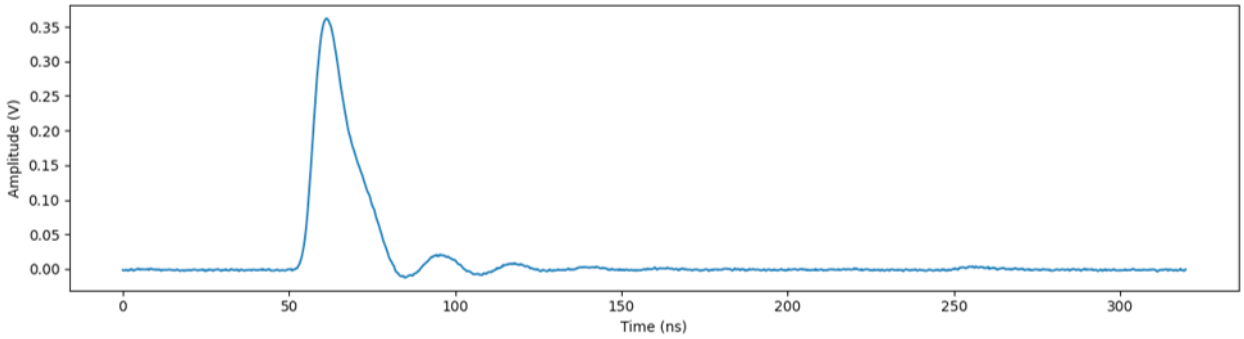

Fig. 8. Random distorted signal representing a high-energy event.

A Python script based on the SciPy library [13] for peak detection has been used to address this issue. Conducting a visual inspection on many randomly selected events flagged as "with pile-up" and "without pile-up" played an important role in fine-tuning the algorithm by adjusting its internal key parameters. Despite the program frequently detecting the initial bump after the main pulse in a distorted sequence, stringent conditions were set to exclude it from being counted as a valid pulse. With the above-described accelerator settings, we observed that approximately 5 to 10% of sequences were flagged as containing pile-ups. Notably, this ratio rapidly deteriorated when increasing the beam intensity.

Figure 9 illustrates examples of sequences sorted by the algorithm developed in this work. Baseline correction was implemented by calculating the mean value of the initial 30 ns data points in each sequence. Incorporating the standard deviation of the mean value was crucial to account for scenarios where a decreasing pulse might occur at the sequence's outset.

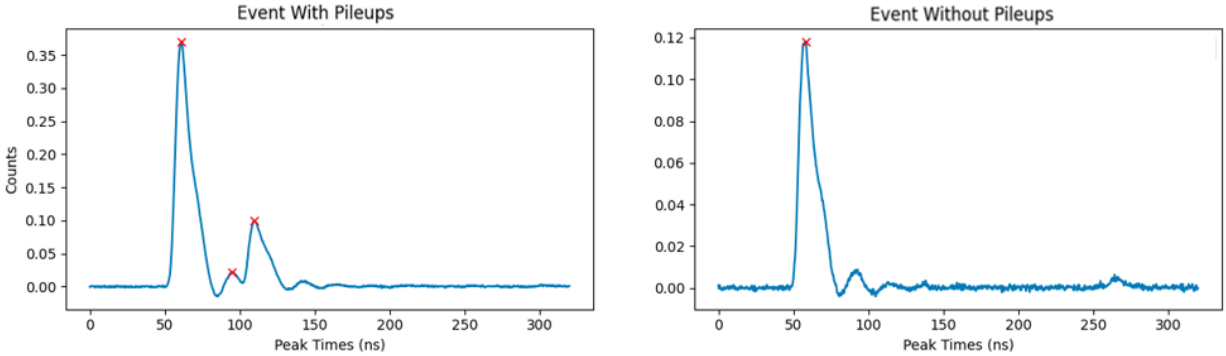

Fig. 9. Examples of signal sequences flagged as « with pile-up » or « without pile-up ». The red crosses are indicating that a pulse was detected by the algorithm.

3.2. Two-dimensional pulse shape discrimination charts

In a liquid scintillator like the BC501A, the discrimination between neutron and photon interactions is achieved through pulse shape discrimination (PSD), which relies on the distinct excitations induced by heavy and light charged particles in the scintillation mixture. Neutron interactions lead to the production in the scintillator of relatively heavy recoil protons, compared to the Compton electrons being generated by the photon interactions. The higher specific ionization (linear energy transfer - LET) of heavier recoil protons in the scintillator results in the creation of higher-energy excited states, causing more of the delayed de-excitation process manifested as fluorescence. The latter is detected by the photomultiplier tube (PMT), and its pulse shape reveals information about the nature of the interacting particle, distinguishing between heavy and light charged secondary particles produced respectively by neutrons and photons.

Specifically, the pulse shape consists of two components: a fast (prompt) component, characterized by a decay time of only a few ns, and a slow (delayed) component, also known as the tail, which can persist for several tens of ns. Neutron interactions, at the origin of relatively heavy charged particles like protons, predominantly contribute to the slow component of the fluorescence. Photon interactions are featuring in contrast much lighter charged particles like Compton electrons and therefore contribute significantly less to the fluorescence light output in the slow component [14].

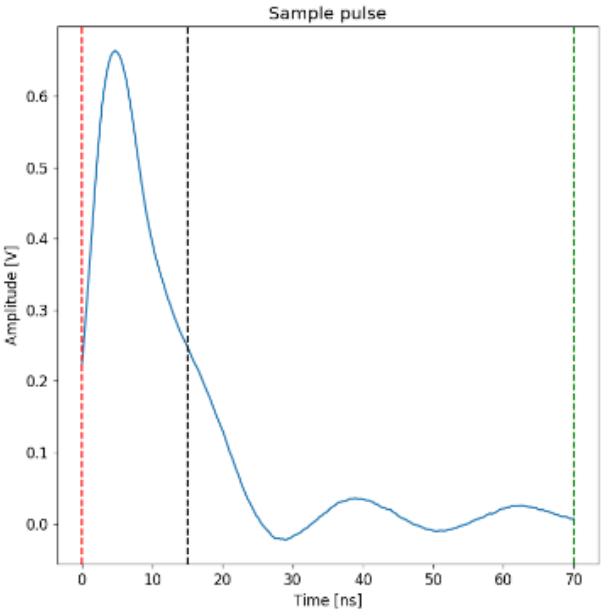

Fig. 10. Unique event with the gates corresponding to the integrals for Q_{tot} (between red and green dashed lines) and for Q_{tail} (between black and green dashed lines).

We based our data analysis on the commonly used charge-comparison method of Heltsley et al. [15]. This PSD method involves the integration via an algorithm of the total charge of each pulse and the integration of the charge from a fixed temporal fraction of each pulse (i.e. either the first fast component or the longest tail component).

This is illustrated in Figure 10 where Q_{tot} represents the total integral charge starting at 35% of the rising time to an optimum endpoint where the slow tail reaches background, and Q_{tail} is an integration of the pulse starting from a selected beginning of the tail to the same endpoint referred to as the tail integral. These windows are spanning over, respectively, 55 and 70 ns. The ratio CCM (discrimination factor or charge comparison method parameter) between the tail integral and the total integral given by Eq. 1 is further used

to separate the proton from Compton electron events originating respectively from neutron and photon interactions in the liquid scintillator. The signals corresponding to photon and neutron interactions can then be separated by plotting the total charge of each pulse against the discrimination factor CCM (scatter-density plots).

$$CCM = Q_{tail}/Q_{tot} \quad \text{Eq. 1}$$

In order to test the pulse shape discrimination method before its further use for the analysis of the data measured using the beam provided by the electron LINAC, preliminary measurements have been first performed in conventional experimental configurations using laboratory well characterized sources with the following main characteristics:

- ^{252}Cf, 5.5x10^{6} neutrons/s
- Am-Be, 1.0x10^{6} neutrons/s
- ^{88}Y gamma source, 90.0 kBq on 09/10/2023

The cumulative total light output of the detector within a pulse was assessed through the total charge, denoted as stated earlier Q_{tot}, acquired by integrating the entire digitized signal across a temporal gate beginning at 35% of the maximum amplitude and spanning a duration of 70 ns. The rationale for employing this brief integration window is related to the necessity to mitigate the potential for pile-up events within the integration timeframe, particularly in environments characterized by high counting rates.

The total charge was calibrated in terms of equivalent electron energy (E_e in MeVee) using Compton electrons induced in the scintillator by γ-rays from ^{22}Na, ^{137}Cs, ^{88}Y, and ^{60}Co sources. Gaussian distribution fits were applied to determine the charge corresponding to the Compton edge energy, which was found to be a fraction of 90% of the maximum height of the Compton distribution. A linear correlation (Eq.2) was assumed between the energy and the charge [16].

$$Q = a(E_e - b) \quad \text{Eq. 2}$$

The calibration curve obtained is shown on Figure 11. The small energy offset ($b = -67$ keVee) takes into account the nonlinearity due to typical quenching effects in organic scintillators for small electron energies.

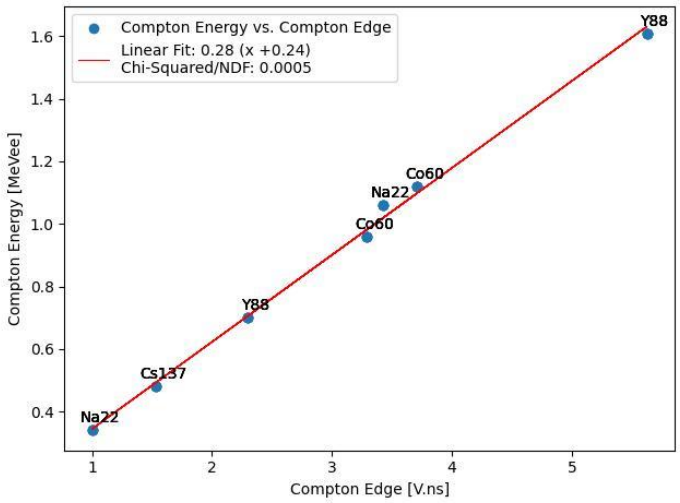

Fig. 11. Linear fit between the Compton energy and the Compton edge for several calibration photon sources.

The PSD scatter-density plots shown in Figures 12 and 13 have been obtained from the measurements with the ^{252}Cf and the Am-Be sources respectively.

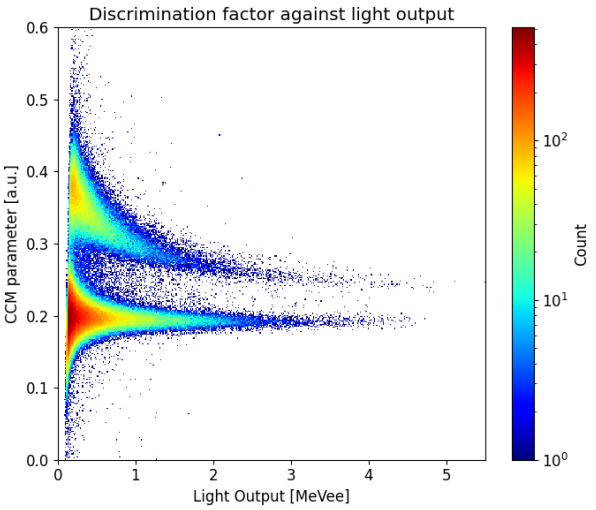

Fig. 12. PSD scatter-density plot for neutrons and photons of a total of 405835 unique events from the ^{252}Cf neutron source.

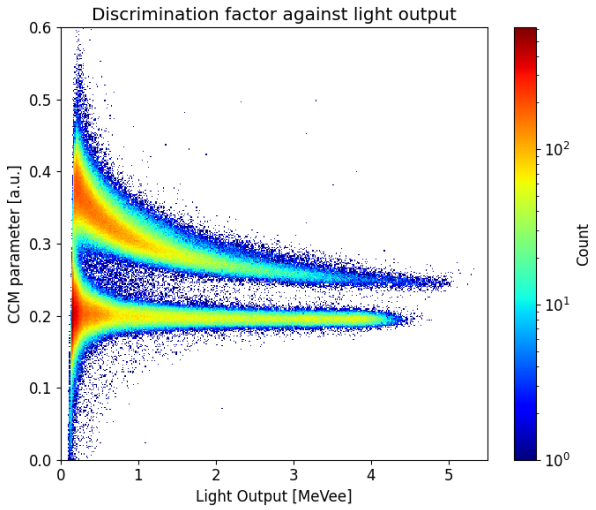

Fig. 13. PSD scatter-density plot for neutrons and photons of a total of 794293 unique events from the Am-Be neutron source.

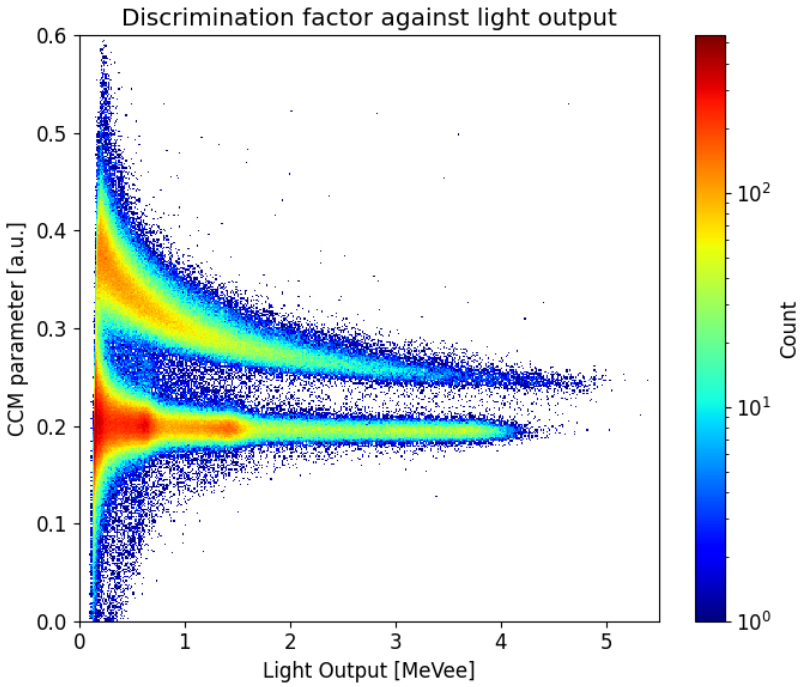

Fig. 14. PSD scatter-density plot for neutrons and photons of a total of 792247 unique events for the configuration combining a Am-Be neutron source and a ^{88}Y photon source, both placed at 10 cm from the detector.

The Am-Be source generates neutrons with energies up to around 10 MeV produced by the following nuclear reaction:

$$^{9}_{4}Be + \alpha \rightarrow n + {}^{12}_{6}C^{*} + Q\,(5.704\ \text{MeV}) \qquad \text{Eq. 3}$$

Photons emitted by this source are associated to the gamma rays from the decay of the excited residual nucleus $^{12}C^{*}$ and explain the extension to higher energies of the photon line, when compared to the chart obtained for the ^{252}Cf source which emits neutrons with a Watt energy distribution peaking around 1 MeV. Good performance remains however achievable thanks to the very fast response of the BC501A scintillator and the short integration time over each particle pulse being used.

It is important to highlight that even with rather high activities such as 16 GBq used in our case for the Am-Be source and being placed close to the detector at around 10 cm, the contribution of the pile-up events is relatively limited at less than 1 %.

Moreover, when increasing the photon contribution by adding a ^{88}Y source to the measurement configuration using the Am-Be neutron source, the pile-up fraction, although increased to 2 %, still remains within reasonable limits. In Figure 14 is shown the discrimination chart obtained for this latter configuration. The additional contributions from photons at 0.898 MeV and 1.836 MeV corresponding to the γ-rays from the decay of ^{88}Y are clearly visible in the lower line representing the signal from photon interactions in the detector.

For the measurements in the beam produced by an electron LINAC one has to deal with a completely different dynamics for data acquisition. Considering the exceedingly high counting rate during the accelerator flash, it becomes very challenging to separate distinct events for charge integration, even within a short duration such as 70 ns. In most cases, minor fluctuations in event pulses lead to pile-up events that are very hard to reject automatically resulting in a broader array of pulses compared to those obtained from a conventional source.

Figure 15 shows the result for the scatter-density plot from pulse shape discrimination obtained by irradiating the tungsten target with the electron beam from the LINAC. During the measurements, the target was exposed to bursts of approximately 1×10^{8} electrons lasting for 3.5 µs, having an end-point energy of 22 MeV. These electron bursts arrive on the target with a frequency of 120 Hz. The lower line represents the photons from the Bremsstrahlung radiation generated by electron interactions in the target. Photoneutrons consequently produced in the target are grouped in the upper line of the two-dimensional plot and the results presented in Figure 15 show that they are mostly emitted at low energies.

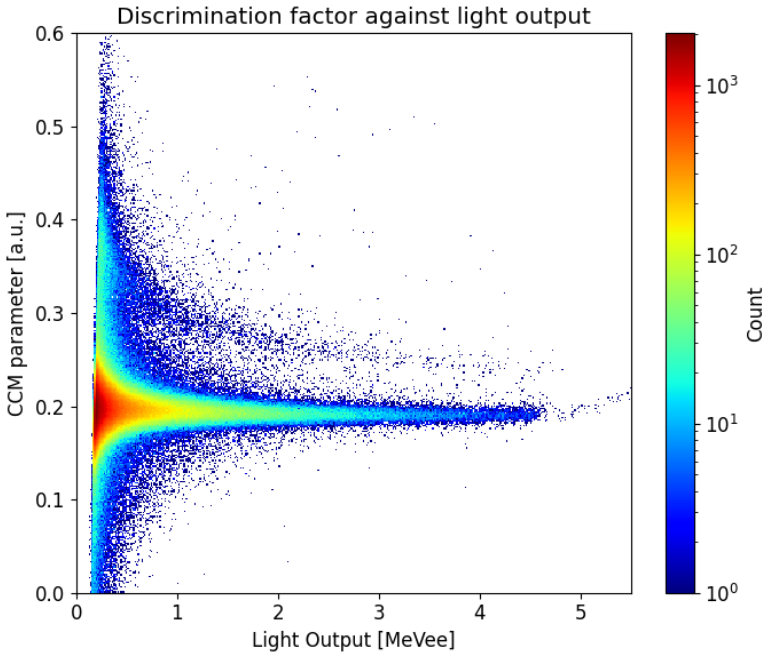

Fig. 15. PSD scatter-density plot of a total of 991673 unique events registered during the irradiation of the tungsten target with 22 MeV electrons from the pulsed LINAC.

In this configuration, approximately 20% of the detected events were identified as pile-up events. While this percentage may appear reasonable at a first glance, it is crucial to emphasize that certain less conspicuous pile-up events remained undetected. This oversight contributes to the overall dispersion of the Pulse Shape Discrimination (PSD) scatter-density plot.

3.3. Experimentally assessed discrimination quality and optimization

Histograms representing the neutron and photon events as a function of the discrimination factor CCM were obtained by projection over the Y-axis of the two-dimensional scatter-density plots presented in the previous section. Neutron and photon events are then represented by two separate peaks as shown in Figures 16-19 for the four above discussed measurement configurations considered in our study (three using neutron sources and the fourth one using the electron beam accelerated by the LINAC).

To quantify the quality of the discrimination achieved, a figure of merit (FoM), defined as the separation of the centroids of the two peaks divided by the sum of their FWHMs [17] is calculated based on the formula:

$$FoM = \frac{\overline{R_n} - \overline{R_\gamma}}{FWHM_n + FWHM_\gamma} \quad \text{Eq. 4}$$

where $\overline{R_n}$ and $\overline{R_\gamma}$ are respectively the mean positions of the neutron and photon peaks, $FWHM_n$ and $FWHM_\gamma$ are the corresponding Full Widths at Half Maximum (FWHM) of the peaks given by the following equation, where σ is the standard deviation.

$$\text{FWHM} = 2\sigma \cdot \sqrt{2 \cdot \ln 2} \quad \text{Eq. 5}$$

The values were obtained from a fit of the distributions with a sum of two Gaussian functions defined by:

$$f_i(R) = a_i \cdot e^{-\frac{(R-R_{0i})^2}{2\sigma_i^2}} \quad \text{Eq. 6}$$

Where $i = n$ or γ, a_i is the amplitude, and R_{i0} is the most probable value.

The figure of merit or degree of neutron-photon separation achievable depends on the energy thresholds applied to plot the histograms of discrimination factor. Highest figure of merits (FoMs) corresponding to the optimal separation of neutron and photon is achieved at high threshold energies. The Q_{tail} and Q_{tot} integration gates were adjusted in order to maximize the figure of merit. On the other hand, the long gate should be as short as possible as mentioned in Section 3.2. As a good compromise to all these respects, 55 ns and 70 ns were chosen respectively for Q_{tail} and Q_{tot} time integration gates. For the following discrimination factor histograms, the energy threshold was set at 1 MeVee.

A statistics associated to the FoM is the neutron rejection ratio (NRR). This quantity was introduced by R.A. Winyard *et al*. [18] and represents the fraction of neutron events being misidentified as photons. Converting the FoM into the NRR is possible in the approximation that photon and neutron peaks are Gaussian. It implies the introduction of a threshold called intersection (I) that separates the photon and neutron events. The optimal threshold, in terms of minimizing the number of misidentifications of either type, is located at an equal number of standard deviations away from each center point $\overline{R_n}$ and $\overline{R_\gamma}$ as previously defined. B.S. McDonald *et al*. [19] further explained this relationship using Eq. 7. The neutron rejection ratio employs the complementary error function, denoted $erfc$. Essentially, this percentage gives the likelihood of misclassifying a neutron event as a photon when its tail-to-total integral falls below this intersection threshold.

This dual-parameter approach improves the FoM by offering a more tangible representation of particle

$$\text{NRR} = \frac{1}{2} \cdot erfc(2 \cdot \sqrt{\ln 2} \cdot FoM) \quad \text{Eq. 7}$$

discrimination performance, especially important where non-Gaussian tails may influence the rejection ratio calculations as in the case of environments with high photon contribution.

Figures 16, 17 and 18 are showing the distributions of the discrimination factors for events from the measurements using the neutron sources (^{252}Cf and Am-Be) and the combination of Am-Be and ^{88}Y gamma sources. They rely on the PSD scatter-density plots shown in Figures 12-14. Finally, the results obtained for the experimental configuration when irradiating the tungsten target by 22 MeV electrons from the pulsed LINAC are presented in Figure 19.

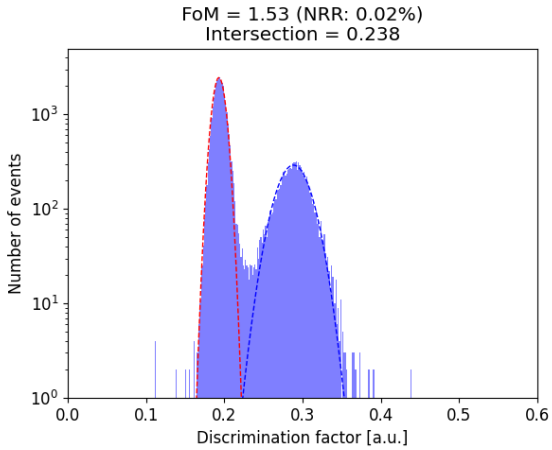

Fig. 16. Discrimination factor histogram for the ^{252}Cf neutron source.

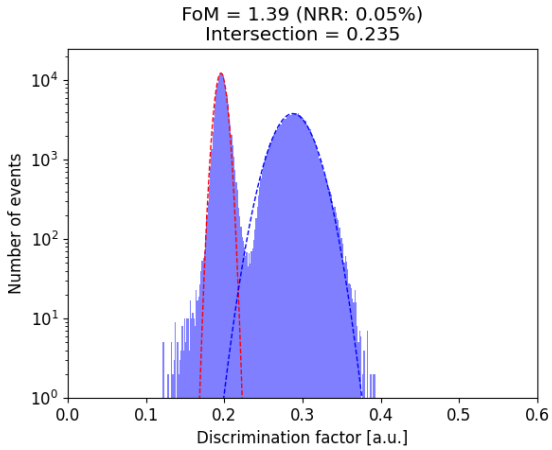

Fig. 17. Discrimination factor histogram for the Am-Be neutron source.

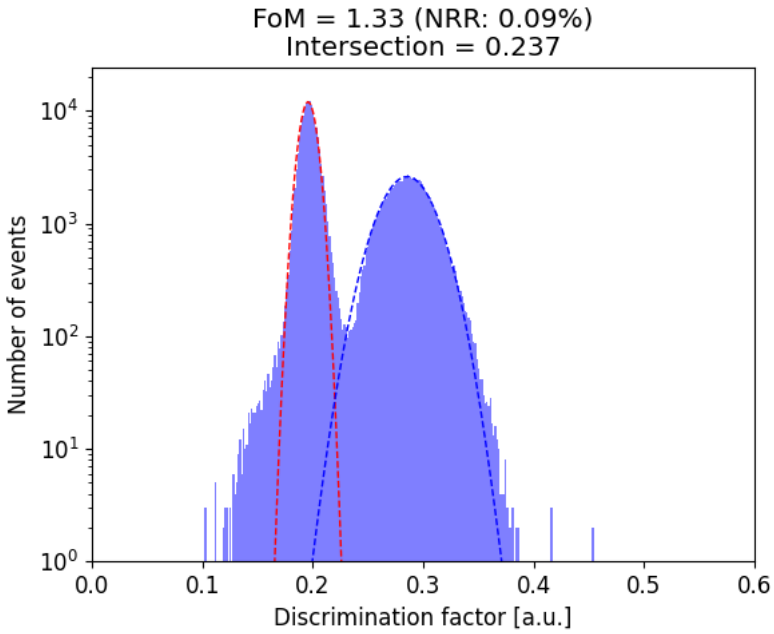

Fig. 18. Discrimination factor histogram for the combined Am-Be neutron source and 88Y photon source.

For the liquid scintillator BC501A used for the measurements with conventional neutron sources, neutron-photon discrimination performance is very high, in line with the similar findings widely acknowledged in the existing literature. In our specific experimental conditions, we measured Figures of Merit (FoMs) of 1.53 and 1.39 with the ^{252}Cf and Am-Be neutron sources respectively. The fact that the Am-Be source is a more potent photon emitter than the ^{252}Cf source explains the observed difference in FoMs between the two configurations. Enhanced FoMs are attainable by extending integration over longer time gates, although this metric tends to decrease in photon-rich environments. The introduction of the ^{88}Y photon source alongside the Am-Be neutron source reduces the FoM to 1.33 due to the broadening of the photon line. The neutron "line" in the PSD scatter-density plot appear somewhat curved rather than straight like the photon line in all acquisitions. This curvature can be attributed to the inherent neutron/gamma discrimination property of the BC-501-A detector. This phenomenon becomes particularly noticeable during irradiations with the Am-Be source, where the energetic nature of the produced neutrons amplifies this effect. This cause the neutron peaks in the discrimination factor histograms to deviate from a Gaussian shape.

For the measurements using tungsten irradiation by 22 MeV electrons from LINAC the obtained FoM value decreases 1.03. As shown in Figure 19, the photon peak becomes significantly wider in this case while the neutron contribution decreases to the baseline. The counting rate for photons is about two orders of magnitude higher than for neutrons and the neutron peak is scarcely discernible.

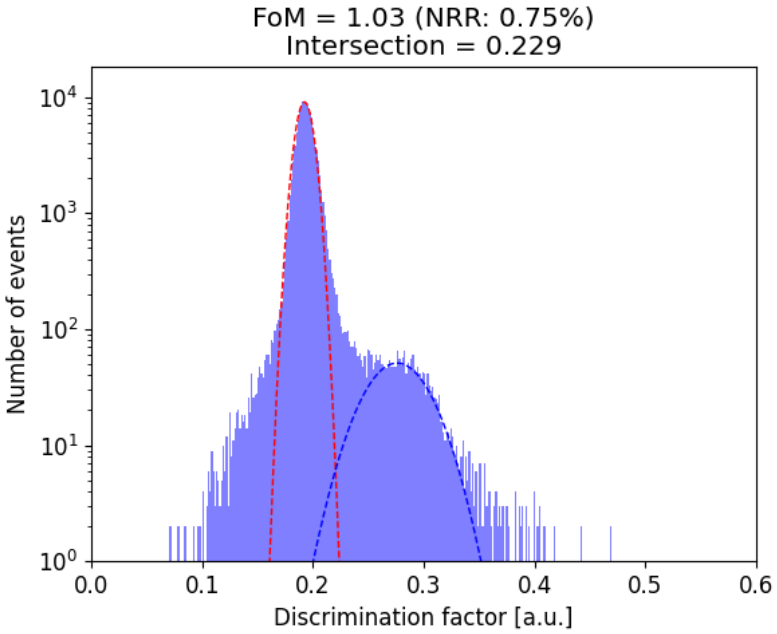

Fig. 19. Discrimination factor histogram for the irradiation of the tungsten target by 22 MeV electrons from the pulsed LINAC.

For the last two discrimination factor histograms, the discrimination factors shoulders is caused by piled-up events that could not be rejected by the pile-up rejection algorithm due to photo-rich environments. This is highlighted by the logarithmic scale used on the number of events axis.

The Neutron Rejection Ratio (NRR) was assessed for the four measurement configurations. Observations revealed a notable increase in the NRR as photon radiation levels increase in the detector's environment. This trend underscores that the efficiency of neutron rejection diminishes in scenarios with elevated photon radiation. Specifically, in the case of tungsten irradiation by 22 MeV electrons this limitation becomes significant as the probability of misidentifying neutrons as photons is 0.75%. This highlights the impact of high photon radiation on the NRR, emphasizing the importance of detector shielding for accurate neutron detection. Our results however show evidence that this performance metric remains promising even in

challenging measurement configurations associated to short-pulsed electron LINAC environments and hold the potential for further improvements through the implementation of more sophisticated post-treatment algorithms.

4. CONCLUSIONS AND PERSPECTIVES

The present work allows significant advancements in the field of high-energy photon interrogation, demonstrating the potential of fast organic scintillators like the BC501A to extend the application of Active Photon Interrogation (API) techniques to the detection of a broader range of illicit materials.

The synchronization of the accelerator with the detector's acquisition system, coupled with a post-treatment algorithm for pile-up rejection, enabled the accurate detection of events exclusively during the short pulses of the accelerator.

Furthermore, our research achieved a notable milestone in discriminating between neutrons and photons through a simple charge comparison method when using linear electron accelerators to generate the photon source. Despite the challenges associated to the very intense photon flux, pulse pile-up and detector saturation, our results demonstrate that the pulse shape discrimination capabilities and rapid time-scale operation of organic scintillators are suitable for effective neutron detection, even in mixed short-pulsed fields of photon and neutron radiation with intense photon flashes.

Future work may consider the integration of machine learning algorithms as very promising tools for further improving the rejection of pulse pile-up and enhancing pulse shape discrimination in these very challenging measurement conditions. Moreover, in order to address the limitation related to the dead time in the present acquisition system during event analog to digital conversion (125 µs for the CAEN DT5743 digitizer used in this study), the adoption of a digital oscilloscope emerges as a potential solution. This could substantially accelerate pulse registration speed, mitigating the time required to accumulate sufficient data statistics. However, it is important to note that this acceleration comes with another drawback when comes to managing the substantial increase in the volume of data collected.

The successful separation of unique pulses from events and the satisfactory discrimination between neutron and photon radiation highlights the robust performance of our approach. These achievements are a solid basis for the use of our method for further applications in the detection of light elements in conventional explosives, narcotics and chemical weapons. As we navigate the initial experimental aspects of detection of photoneutrons produced by high-energy photons, this work establishes a solid foundation for the development of a promising new detection method for illicit materials. The outcomes of this study pave the way for further research and technical refinements, contributing to the advancements in nuclear physics applications for security and materials detection.

ACKNOWLEDGMENTS

Authors would like to acknowledge the financial support provided by the French National Laboratory of Metrology and Testing. We also express our gratitude to the CEA laboratory for activity metrology, particularly M. Cheick Thiam for his contribution to the calibration of our detector.

REFERENCES

1. Y. Zhao, T. Cui, Y. Yang, "The design of a photoneutron source for narcotic drugs detection in a large-truck," in Proc. 2017 IEEE Nuclear Science Symposium and Medical Imaging Conference (NSS/MIC 2017), Atlanta, Georgia, October 21–28, 2017.
2. C.L. Fontana, A. Carnera, M. Lunardon, F. Pino, C. Sada, et al., "Detection system of the first rapidly relocatable tagged neutron inspection system (RRTNIS), developed in the framework of the European H2020 C-Bord project," Physics Procedia, vol. 90, pp. 279-284, 2017.

3. M. Gmar, E. Berthoumieux, S. Boyer, F. Carrel, D. Doré, et al., "Detection of nuclear material by photon activation inside cargo containers," in Proc. SPIE Defense and Security Symposium, Orlando, Florida, April 17–21, 2006.
4. C. Besnard-Vauterin, V. Blideanu, B. Rapp, "Development of a new method for the detection of illicit materials based on the active interrogation method and photoneutron spectrometry," in Proc. of 8th Int. Conf. Advancements in Nuclear Instrumentation Measurement Methods and their Applications (ANIMMA), Lucca, Italy, June 12–16, 2023.
5. K.W. Habiger, J.R. Clifford, R.B. Miller, W.F. McCullough, et al., "Explosives detection with energetic photons," Nucl. Instrum. Methods Phys. Res. B, vol. 56-57, no. 2, pp. 834-838, 1991.
6. C. Besnard-Vauterin, V. Blideanu, B. Rapp, "Development of a new method for neutron spectra analysis based on a deep learning algorithm for the detection of illicit materials," in Proc. of the International Conference on Mathematics and Computational Methods Applied to Nuclear Science and Engineering, Niagara Falls, Ontario, Canada, August 13-17, 2023.
7. A.J. Jinia et al., "Measurement of Photoneutrons from Depleted Uranium and Comparison Study Using MCNPX-PoliMi," Nuclear Science and Engineering, 2023.
8. A. Danagoulian et al., "Prompt neutrons from photofission and its use in homeland security applications," in 2010 IEEE International Conference on Technologies for Homeland Security (HST), Waltham, MA, USA, pp. 379-384, 2010.
9. A.J. Jinia et al., "An Artificial Neural Network System for Photon-Based Active Interrogation Applications," IEEE Access, vol. 9, pp. 119871-119880, 2021.
10. M. Moszynski et al., "Study of n-γ discrimination with NE213 and BC501A liquid scintillators of different size," Nucl. Instrum. Methods Phys. Res. A, vol. 350, p. 226, 1994.
11. Photomultiplier tubes and assemblies, HAMAMATSU Company.
12. Photomultiplier Tubes Handbook, HAMAMATSU Company.
13. P. Virtanen, R. Gommers, T.E. Oliphant, M. Haberland, T. Reddy, et al., "SciPy 1.0: Fundamental Algorithms for Scientific Computing in Python," Nature Methods, vol. 17, no. 3, pp. 261-272, 2020.
14. J.B. Birks, "The Theory and Practice of Scintillation Counting," Pergamon Press, Oxford, pp. 219-227, 392-394, 1964.
15. J.H. Heltsley, L. Brandon, A. Galonsky, et al., "Particle identification via pulse-shape discrimination with a charge-integrating ADC," Nucl. Instrum. Methods Phys. Res. A, vol. 263, pp. 441-445, 1988.
16. G. Dietze, H. Klein, "Gamma-calibration of NE 213 scintillation counters," Nucl. Instrum. Methods Phys. Res. A, vol. 193, no. 3, pp. 549-556, 1982.
17. G.F. Knoll, "Radiation Detection and Measurement," 3rd edn., Wiley, New York, p. 680, 1989.
18. R.A. Winyard, J.E. Lutkin, G.W. McBeth, "Pulse shape discrimination in inorganic and organic scintillators. I," Nuclear Instruments and Methods, vol. 95, no. 1, pp. 141-153, 1971.
19. B.S. McDonald, M.J. Myjak, M.A. Zalavadia, J.E. Smart, J.A. Willett, P.C. Landgren, C.R. Greulich, "A wearable sensor based on CLYC scintillators," Nucl. Instrum. Methods Phys. Res. A, vol. 821, pp. 73-80, 2016.